Drosophila larval models of invasive tumourigenesis for in vivo studies on tumour/peripheral host tissue interactions during cancer cachexia.

Joseph A. Hodgson[1‡], Jean-Philippe Parvy[1‡], Yachuan Yu[1], Marcos Vidal[1] and Julia B. Cordero[1,2].

1. CRUK Beatson Institute. Institute of Cancer Sciences. University of Glasgow. Garscube Estate, Switchback Road, G61 1BD. Glasgow, U.K.
2. Wolfson Wohl Cancer Research Centre. Institute of Cancer Sciences. University of Glasgow. Garscube Estate, Switchback Road, G61 1QH. Glasgow, U.K.

‡ Equally contributing authors

* Corresponding author: julia.cordero@glasgow.ac.uk

Abstract

Cancer cachexia is a common deleterious paraneoplastic syndrome that represents an area of unmet clinical need, partly due to its poorly understood aetiology and complex multifactorial nature. We have interrogated multiple genetically defined larval *Drosophila* models of tumourigenesis against key features of human cancer cachexia. Our results indicate that cachectic tissue wasting is dependent on the genetic characteristics of the tumour and demonstrate that host malnutrition or tumour burden are not sufficient to drive wasting. We show that JAK/STAT and TNF-α/Egr signalling are elevated in cachectic muscle and promote tissue wasting. Furthermore, we introduce a dual driver system that allows independent genetic manipulation of tumour and host skeletal muscle. Overall, we present a novel *Drosophila* larval paradigm to study tumour/host tissue crosstalk in vivo, which may contribute to future research in cancer cachexia and impact the design of therapeutic approaches for this pathology.

Keywords: *Drosophila* larvae; *Ras*, *Scribble;* dual driver system; cancer cachexia.

Introduction

Cancer is one of the leading causes of death worldwide. Even though the devastating effects of cancer are often linked to non-tissue-autonomous consequences of tumour burden, the understanding of the interactions between tumours and host tissues remains incomplete. One such outcome of these interactions is the onset of cancer cachexia, a paraneoplastic syndrome defined as the “loss of skeletal muscle mass (with or without loss of fat mass) that cannot be fully reversed by conventional nutritional support and leads to progressive functional impairment” [1].

Cachexia is a multifactorial and multi-organ pathology, which is thought to cause up to 30% of late-stage cancer-related deaths [2, 3]. Clinical manifestations of cachexia include asthenia, anorexia, significant loss of body fat and muscle, metabolic deregulation, abdominal fluid accumulation, systemic inflammation, and immune infiltration of various tissues, among others [4, 5]. Cachexia is identified in up to 80% of advanced-stage cancer patients [6], and reduces tolerance to treatment, therapeutic response, patient quality of life, and survival [7, 8]. Nevertheless, there is no clear gold standard therapy for cachexia, and it therefore represents a major unmet clinical need [9].

One of the problems at the root of the dearth of therapeutic interventions for the treatment of cachexia is the fact its aetiology is poorly understood. Cachexia is a multifactorial condition further complicated by the heterogeneity of the general population, tumours themselves, and the therapies used to treat them. This is evidenced by observations that patients with apparently similar tumours can have very different responses in terms of developing cachexia [10], and the fact cachexia is most frequently associated to various metastatic tumour types, such as pancreatic, lung, gastric, and renal-cell cancers [11-13]. These characteristics are maintained in mouse models, where histologically similar tumours result in distinct cachectic outcomes [14], and in tumour cell lines from different sources, which have widely variable effects [15]. Given the predisposition of certain tumour types for the induction of cachexia, there are likely to be one or more molecular mechanisms that underpin whether a tumour will be cachectogenic, yet the heterogeneity and complexity of higher models makes the identification of pro-wasting mechanisms very difficult.

Drosophila has been successfully utilised as a model system to understand the growth and development of cancer [16-18], and to investigate the communication between host tissues and the tumour itself [19-22]. Several adult *Drosophila* tumour models have been used to identify tumour-secreted factors contributing to peripheric tissue wasting [23, 24], making tumours refractory to the action of pro-wasting factors [25] and driving host anorexia [26]. A *Drosophila* larval model of high-sugar diet (HSD)-enhanced tumourigenesis identified important metabolically induced molecular changes within tumours driving muscle wasting [27]. While these studies have provided invaluable insight into tumour driven mechanisms of cancer cachexia, less is known about the molecular changes occurring within peripheric tissues and their functional role in tumour-driven host tissue wasting.

Here, we analyse several genetically defined larval *Drosophila* tumour models and show that only some of them recapitulate molecular and phenotypic aspects of cancer cachexia. We closely characterize the aetiology of the process and define primary versus secondary factors contributing to cachexia. Our results unambiguously point to the genetic characteristics of the tumour, rather than tumour burden or anorexia, as key primary determinants in the development of cachexia. We analysed transcriptional changes in wasting muscles and identify molecular pathways involved in wasting. Importantly, we establish a novel *Drosophila* larval model of cancer cachexia using a dual-driver system that allows parallel and independent genetic manipulation of muscle and tumour and which would facilitate studies of host-tumour interactions in cachexia and beyond.

Results and Discussion

Cachexia is dependent on tumour genotype

Loss of function mutations in cell polarity genes can induce neoplastic tumour formation in larval imaginal discs [16, 28, 29]. These transformed neoplastic epithelial discs result in larval developmental delay and eventual death [16, 28, 29]. Expression of oncogenic Ras^{V12} in these neoplastic tumours creates more aggressive invasive tumours that are able to invade distal tissues [18, 30]. Hyperplastic tumours can also be generated in *Drosophila* by hyperactivation of the Hippo pathway [24, 31]. As in human cancer patients, adult *Drosophila* tumour models has revealed heterogenous wasting phenotypes dependent on tumour genetics and location as well as dietary conditions [23, 24, 27]. Therefore, to identify some key features driving cachexia-like tissue wasting by tumours, we analysed the impact on muscle wasting of genetically distinct tumours in otherwise similar conditions.

We generated different tumour types in larval imaginal discs in order to assess whether cachectic phenotypes could be observed in these animals and compared tumour-bearing and tumour-free animals. We quantified three phenotypic parameters associated with the human syndrome: tumour burden, cachexia-like tissue wasting, and the presence of lipid droplets within muscles (Figure 1A). The latter was used as a parallel of the characteristic intramyocellular lipid droplet (IMLD) accumulation observed in human cancer cachexia [32]. Cachectic muscle wasting was quantified by assessing the percentage coverage of the cuticle by body wall muscle, tumour burden by assessing imaginal disc volume, and IMLDs by quantifying the frequency of lipid droplets per unit area of the 5th segment of the 7th ventral muscle (Figure 1A).

We induced hyperplastic wing disc tumours through expression of constitutively active Yorkie (Yki), Yki^{S168A} using the *rotund-gal4* driver. To model non-invasive neoplastic tumours we used homozygous *discs large* (*dlg*) mutant animals, $dlg^{40.2}$. Invasive neoplastic tumours were produced either through the formation of eye disc-specific *scribbled* mutant clones ($scrib^{1}$) expressing Ras^{V12} (Ras^{V12}, $scrib^{1}$) or expression of Ras^{V12} and $scrib^{IR}$ under the control of *hedgehog-Gal4* (Ras^{V12}, $scrib^{IR}$) (Figure 1 B-F and Figure S1).

As previously demonstrated, neoplastic tumours induce developmental delay [33] (Figure S1). A mild muscle wasting phenotype was detected at 9 days after egg deposition (AED) in delayed animals with Ras^{V12}, $scrib^{1}$ or Ras^{V12}, $scrib^{IR}$ invasive neoplastic tumours as quantified by the coverage of the larval cuticle by body wall muscle (Figure 1K). At 12 days AED a strong muscle wasting phenotype could be observed in these animals, while larvae with non-invasive neoplastic $dlg^{40.2}$ tumours showed a milder, though significant, wasting phenotype (Figure 1G-K and Figure S2). The characteristic IMLD phenotype seen in the wasting muscle of cachectic patients was recapitulated in the wasting muscle of cachectic larvae, although this phenotype was much milder in $dlg^{40.2}$ tumour-bearing larvae at 12 days AED and showed a non-significant trend (Figure 1L-P and Figure S3). Developmental delay alone was not sufficient to induce wasting, as tumour-free developmentally delayed *ecdysoneless* mutant (ecd^{1}) larvae showed neither muscle wasting nor IMLD formation (Figure 1K, P and Figure S2, S3). Consistent with a previous report, hyperplastic Yki^{S168A} imaginal disc tumours were not cachectogenic [24], and showed neither larval muscle wasting nor IMLD formation (Figure 1H, K, M,M", P).

Our results suggest that the genetic characteristics of the tumour, which define the tumour phenotype as either neoplastic or hyperplastic, and invasive or non-invasive, determine the presence and degree of cachectic wasting, respectively. However, Yki^{S168A} tumours did not induce the strong developmental delay seen in neoplastic tumour genotypes (Figure S1, S3). Even though Yki^{S168A} tumours developed to a much larger size than any other tumour at six days AED (Figure 1F and Figure S1), wasting only becomes evident in the context of extensive developmental delay, and in tumours significantly larger than those of the oldest occurring Yki^{S168A} larvae (Figure 1B-K and Figure S1, S2). It was therefore conceivable that longer developmental timing in the context of Yki^{S168A} tumour burden might ultimately lead to cachexia. Indeed, hyperactivation of *Yki* in a model of adult intestinal tumourigenesis leads to periferal host tissue wasting [23].

To test such possibility, we generated hyperplastic Yki^{S168A} tumours in the background of the ecd^{1} mutation, in order to produce large hyperplastic tumours in the context of developmental delay. We compared these tumours to cachectogenic Ras^{V12}, $scrib^{1}$ tumours of the same size (Figure 2A, B, G), and found that Yki^{S168A},

ecd^{1} animals displayed no cachectic phenotypes of muscle wasting (Figure 2 C, D, H) or IMLD formation (Figure 2E-F', I).

Altogether, these results demonstrate that tumour burden in the context of developmental delay was not sufficient to drive cachexia and that it is the genotype of the tumour, which is critical to the presentation of wasting. This is consistent with observations in human patients, where specific cancer types such as gastric and pancreatic cancers have a very high prevalence of cachexia (85% and 83% respectively) [13] and more aggressive tumours are associated with the presentation of wasting even when small in size [12, 34], [35].

Starvation and liquid retention are not sufficient to drive cachexia.

Anorexia can drive tissue wasting, and is one of the main clinical manifestations of cachexia [4]. A recent adult eye tumour model in *Drosophila* revealed conserved mechanism by which pro-cachectic tumours induce anorexia, pre-ceding host tissue wasting [26] However, anorexia is not considered a primary driver of cancer cachexia, as reversing it is not sufficient to fully rescue the loss of tissue [36, 37]. During normal development, *Drosophila* larvae feed almost constantly up until the wandering L3 stage. Given larvae stop feeding at the end of the L3 stage and developmentally delayed larvae persist in this stage, we next considered the possibility that the muscle wasting seen in tumour-bearing larvae could be a result of prolonged starvation.

To test our hypothesis, we quantified the amount of food ingested in 30 minutes at different time points by control w^{1118} and *ecd*^{1} larvae, and larvae with *Yki*^{S168A}; *dlg*$^{40.2}$; *Ras*^{V12}, *scrib*^{1} or *Ras*^{V12}, *scrib*^{IR} tumours (Figure 3A). As expected, larval feeding was decreased by the late L3 stage at 6 days AED (Figure 3B). However, in developmentally delayed larvae, no differences in the levels of feeding were observed past 8 days AED, where all larvae analysed, including tumour-free developmentally delayed *ecd*^{1} larvae that do not undergo muscle wasting, had negligible food intake (Figure 3B). Forced starvation of *ecd*^{1} larvae was not sufficient to drive wasting either (data not shown). We next examined the feeding behaviour of *Yki*^{S168A}, *ecd*^{1} animals in the same manner, and found no differences in food intake between non-wasting *Yki*^{S168A}, *ecd*^{1} animals and cachectic larvae with *Ras*^{V12}, *scrib*^{1} tumours (Figure 3C). Altogether, these data demonstrate that starvation is not

sufficient to induce muscle wasting in the context tumour burden in these larval models.

Abdominal fluid accumulation is often present in cachectic cancer patients [4]. Similarly, bloating is a phenotype commonly associated with tumour-bearing larvae. Bloating is essentially the result of fluid retention, which generates an oedema-like phenotype where the larval cuticle, and therefore the body wall muscle, becomes stretched. Developmentally delayed tumour-bearing larvae contain a much larger amount of haemolymph than wild-type larvae [19], which gives rise to the characteristic 'giant larvae' phenotype seen in these animals.

Bloating can be induced in larvae carrying transheterozygous mutations for a regulator of BMP signalling, *larval translucida* (*ltl)* [38]. We found that ubiquitous expression of an RNAi for *ltl* (ltl^{IR}) using a *tubulin-Gal4* driver (*tub>Gal4*) recapitulated the bloating phenotype observed in *ltl* mutants, allowing the assessment of body wall muscle in tumour-free, bloated larvae (Figure 3D-L). To ensure the duration of the bloating time was consistent between genotypes, ltl^{IR} overexpressing larvae were examined at seven days AED to match the time Ras^{V12}, $scrib^{1}$ animals spent in the bloated stage by twelve days AED (Figure 3F-I). Past this seven-day time point ltl^{IR} larvae became much more distended than tumour-bearing animals, and some lethality occurred (data not shown). We saw no cachectic phenotypes in ltl^{IR} larvae (Figure 3M-R", T). These results suggest that, as in the case of starvation, the mechanical stress caused by liquid retention is not sufficient to drive the body wall muscle wasting observed in cachectic tumour-bearing animals.

Inflammation and JAK/STAT signalling is elevated in cachectic larval models.

$Scrib^{-/-}$,Ras^{V12} imaginal disc tumours induce cachexia when transplanted into adult hosts through ImpL2 secretion [24]. We therefore tested the involvement of *impL2* in $scrib^{IR}$,Ras^{V12} larval tumours driven by *hh-gal4* (Figure 1K, L and Figure S1J). Even though overexpression of *impL2* RNAi in this setting caused strong reduction of *impL2* in the tumour (Figure S4A), we did not observe suppression of skeletal muscle wasting (Figure S4B). A similar result was reported in a larval tumour model of diet-induced cancer cachexia [27].

To investigate which factors might be driving the cachectic wasting observed in our larval models we performed RNA sequencing (RNAseq) on the cuticles of wild

type and *Ras*^{V12}, *scrib*^{1} tumour-bearing larvae. Pathway and gene ontology analysis revealed significant deregulation of stress and starvation response genes, metabolic genes, and inflammation and immune regulatory genes within cachectic muscle of tumour bearing larvae (Figure 4A-C and Table S1).

Consistently with the developmental arrest displayed by tumour bearing larvae, we observed a reduced expression of genes involved in ecdysteroid metabolism and response. We also observed a dramatic decrease in several metabolic processes involved in critical cellular functions. Importantly, genes related to mitochondrial ATP synthesis, glucose metabolism and amino acid synthesis were downregulated, recapitulating important features of the human condition as well as other cachectic models [39-43].

RNAseq analysis of wasting muscles also revealed upregulation of pathways involved in protein degradation, the response to starvation and oxidative stress (Figure 4B, C). Trypsin-like cysteine/serine proteases, suggested to be mediators of autophagy, were strongly upregulated in wasting muscles (Figure 4C). In addition, glutathione metabolism and disulphide bond formation were both increased suggesting that during wasting, muscles have to face a strong oxidative stress. Ubiquitin driven protein degradation has also been reported to be a driver of muscle wasting in both sarcopenia and cancer-induced cachexia (Sukari et al, 2016). Amongst the proteins involved in this process, the F-BOX ubiquitin ligase family member Atrogin-1 seems to be an important player in this muscle degradation process [44]. Interestingly, the closest fly *Atrogin-1* homologous gene*, CG11658*, was upregulated in our RNAseq analysis (Table S1) suggesting a potential further analogy with the human condition. Finally, conserved signalling pathways mediating the cellular response to inflammatory cytokines were increased in wasting muscles, including multiple targets of the Janus Kinase/Signal Transducer and Activator of Transcription (JAK/STAT) signalling pathway (Figure 4D). This matches well with mammalian studies that have implicated JAK/STAT signalling in cachectic muscle wasting, either through the autonomous action of JAK/STAT signalling in the muscle [45-47] or the systemic action of the JAK/STAT pathway ligand IL-6 [41, 48-52].

TNF-α was originally known as the ‘cachectic hormone’. Systemic increase in TNF-α and IL-6 are hallmarks of cancer cachexia [1]. However, anti-TNF-α therapies have been used for the treatment of cancer cachexia without much success [53, 54]. Interestingly, the gene encoding for Wengen (*wgn*), a *Drosophila* TNF-α/Egr receptor

[55, 56] and downstream JNK singling were also upregulated in wasting muscles (Table S1). Altogether, these data suggest that cachectic larval tumour models recapitulate multiple cellular and molecular manifestations of the human syndrome. In particular, the conserved activation of JAK/STAT and TNF-α signalling in cachectic muscles recapitulates the 'high inflammation' hallmark of cancer cachexia [52, 57, 58].

Establishing a dual-driver system to study tumour/host interactions in cancer-induced cachexia

We next set up a *Drosophila* larval model carrying a dual driver system (DDS) that would allow concomitant, yet independent, genetic modifications of tumour and peripheral tissues. To achieve this, we used the *Neurospora crassa* derived QF/QUAS/QS system [59] to generate RFP labelled *scrib*^{1}; *Ras*^{V12} invasive tumours within the larval eye antennal imaginal disc while sparing the *Gal4/UAS* [60] system to express transgenes of interest in the body wall muscles (Figure 5A, B). Consistent with our findings in the conventional *scrib*^{1}; *Ras*^{V12} tumour model (Figure 1), tumours generated using our DDS system led to sever hyperplasia of the eye imaginal discs, larval developmental delay and progressive muscle wasting (Figure 5B-D and Figure 6E, H and K). Furthermore, molecular assessment by RT-qPCR confirmed upregulation of the JAK/STAT signaling target *Socs36E*, *wgn* and *CG11658/Atrogin-1* expression in muscles from animals with DDS generated *scrib*^{1}; *Ras*^{V12} clones.

Muscle autonomous JAK/STAT and TNF-α signalling drive tumour-induced tissue wasting in *Drosophila*.

Given the recognised importance of TNF-α and JAK/STAT signalling in human cancer cachexia [1], as a proof-of-principle, we used our DDS system to assess the functional role of these pathways in muscle wasting upon tumour bearing. To achieve this, we overexpressed RNA interference (RNAi) for *stat* and *wgn,* in the muscle of *scrib*^{1}; *Ras*^{V12} tumour bearing larvae. Knocking down either gene impaired progressive muscle wasting in tumour bearing animals (Figure 6D-K) suggesting that activation of JAK/STAT and TNF-α signalling in skeletal muscle of tumour bearing larvae contributes to muscle wasting induced by tumour in this larval model. Future studies would explore the origin of the signals activating JAK/STAT and TNF-α

signalling in cachectic muscles, a potential interconnection between these two inflammatory pathways and the downstream molecular mechanisms through which they promote muscle degradation.

Altogether, we present previously uncharacterized models of tumour induced cachexia in *Drosophila* and develop a paradigm to investigate tumour/skeletal muscle crosstalk during cachexia, which may be also adapted for additional studies on tumour/host interactions in vivo.

Materials and Methods

Drosophila Stocks

A list of all fly stocks and the full genotypes of experimental crosses presented here can be found in Table S2.

The *QUAS-Ras*^{V12} fly line has been generated for this study. Briefly, *Ras*^{V12} was PCR amplified and cloned into a *pQUAST* vector using standard experimental procedure described in [59]. The *pQUAST-Ras*^{V12} construct was sent to Rainbow Transgenic Flies, Inc for injection. Transgenic flies carrying *QUAS-Ras*^{V12} on the third chromosome where used for recombination and for experiments.

Fly Husbandry and Genetics

All crosses were kept in temperature-controlled incubators with a 12-hour light/dark cycle and raised on standard fly medium. Crosses were generally performed at 25°C, apart from *ecd*^{1} larvae in Figures 1 and 3 and Figures S1-3, and *Ras*^{V12}, *scrib*^{1} and *Yki*^{S168A}, *ecd*^{1} larvae shown in Figure 2. These crosses were maintained at 22°C for 4 days AED, and then shifted to 29°C to induce *ecd*^{1}–dependent developmental delay.

Immunofluorescent Staining

Cuticles and tumours were dissected on Sylgard plates in 1X PBS, and subsequently fixed on the plate in 4% formaldehyde (Polysciences, Inc) for 30-40 minutes. After fixation tissues were transferred to a nine-well glass dissection plate for three wash steps of 15 minutes, on an orbital shaker at 80rpm.

Cuticles were washed and stained in 0.05% Saponin in PBS (PBSS), while tumours were washed and stained in 0.1% Triton X-100 (PBST). Cuticles were stained overnight at 4°C with DAPI, Phalloidin-488 (Invitrogen) at 1:100, and LipidTOX Deep Red (Thermofisher Scientific) at 1:500. No secondary staining antibody was performed, and cuticles were washed 3 times in PBSS before mounting on glass slides in Vectashield mounting media without DAPI (Vector Laboratories, Inc.). Tumours were stained overnight at 4°C with DAPI, washed three times in PBST

and mounted on glass slides with a spacer in Vectashield mounting media without DAPI.

F-actin in Figure 4 was stained with Rhodamine Phalloidin (Invitrogen) at 1:100, and PBST was used instead of PBSS.

Tumours stained for cell death included Rabbit anti-Dcp-1 (Cell Signalling) at 1:200 and DAPI in the primary staining, and after washing a secondary incubation at room temperature was performed with anti-Rabbit-594 (Invitrogen). Tumours were then washed and mounted as previously described.

Imaging and Image Processing

All immunofluorescent images were captured on a Zeiss 710 confocal microscope system. Brightfield images were captured on a Leica M205 FA microscope with Leica DFC 500 camera. Image processing was carried out in ImageJ and figure panels were created in Adobe Photoshop CS5.

qPCR

RT-qPCRs were done on 2-4 biological replicates. Each sample/biological replicate was prepared with tissue from 5-10 larvae. Samples were homogenised using a pestle and mortar, and RNA was extracted using QIAGEN RNA extraction columns with DNAse treatment. cDNA conversion was performed using the High-Capacity cDNA reverse transcription kit (Applied Biosystems). SYBR Green FastMix Low ROX (Quanta Bio) was used for qPCRs. The expression of target genes was assessed relative to the expression of the *RPL32* housekeeping gene, with a series of 10-fold sample dilutions used to produce a standard curve to quantify expression. qPCR was performed on Applied Biosystems 7500 Fast Real Time PCR machine and analysed using the system software. Melt curves were generated for the first use of each primer pair to ensure no primer-dimer or multiple product formation occurred. Primer pairs used can be found in Table S3.

Quantification of the percentage of body wall muscle covering the cuticle

To quantify systemic body wall muscle wasting in larvae the following method was developed, using ImageJ software. LSM Z-stack tile-scans of whole cuticles taken at 10X were analysed. Images underwent maximal Z-projection, channels were merged into a composite image, and then the composite was stacked to an RGB image. The outline of the cuticle was then manually delineated, and the area of this selection was measured in pixels, to provide the value for the area of the whole cuticle. The area outside this selection was then cleared, to ensure that no signal outside of the specific area of interest was quantified. Actin in muscle was stained with phalloidin, with signal intensity presented in ImageJ's standard green look-up table. The Colour Threshold tool was then used to detect the green pixels that represented the actin in muscle. The Hue slider was set to include only the green region of the colour spectrum, and the Brightness slider was adjusted to alter the threshold call to remove any background staining. Once muscles were highlighted, this area was selected and measured in pixels. The percentage coverage of the cuticle by muscle was then calculated from these figures by dividing the value for total pixel area of muscle by the value for total pixel area of the whole cuticle and multiplying by 100.

Quantification of lipid droplet frequency in ventral muscle

To provide a quantitative measure of the lipid droplet phenotype in wasting muscle the following method of quantifying the frequency of lipid droplets observed in muscle was developed, using the ImageJ software. LSM Z-stacks of the 5th segment of the 7th ventral muscle underwent maximal Z-projection, and the channels were merged to form a composite image. The outline of the muscle was manually delineated, and the outline saved to the Region of Interest (ROI) manager. The area of this selection was then measured in pixels and recorded. The channel for LipidTOX dye that stained lipid droplets was then isolated, and the channel converted to an RGB image. The ROI manager of the muscle outline was used to highlight the region of the image previously selected, and all areas of the image outside of this region were excluded. The number of lipid droplets in the muscle was then calculated using the Analyse Particles tool, with settings of Size: 1-3μm, and Circularity: 0.30-1.00. The number of lipid droplets was then divided by the area of muscle in pixels, to provide a comparable measure of the frequency of lipid droplets per unit area of muscle.

Quantification of Tumour Volume and Tumour Cell Death

The Volocity 3D image analysis software (Volocity 6.3.0, Quantitation [Analysis 2D, 3D, 4D] + Base Package) was used in the quantification of tumour volume. Tumour images were cropped to include only the individual tumour, and the software was used to calculate tumour volume. Tumour volume was determined based on the quantification of the total volume of DAPI signal in the LSM Z-stack. The 'Fill Holes in Object' plugin was utilised to ensure that the small spaces between nuclei were included in the quantification for a more accurate assessment of total tumour volume. This quantification process produced a raw data table listing the volume of each surface identified in the image of the tumour. The total volume was then calculated by identifying the sum of all the surfaces identified in each tumour image, using the Volocity results Analysis package.

To quantify cell death tumours were stained with DAPI, and for cells undergoing apoptosis with a marker of cell death, Dcp-1. Tumour volume was quantified as above. The volume of Dcp-1 staining representing cell death was also quantified as described, with an additional filter applied to only quantify the volume of cell death staining that was directly colocalised with DAPI staining. This ensured that the only cells included in the quantification of cell death were present in both the tumour volume quantification, and positive for the cell death marker. The total volume of the whole tumour (DAPI) and total volume of cell death (Dcp-1) were calculated separately using the Analysis package, as previously described. The percentage of tumour cell death was then calculated from these figures by dividing the total volume of dying cells positive for Dcp-1 by the total tumour volume and multiplying by 100.

Larval feeding assessment

Fly food made in the Beatson Central Services unit was melted in a microwave. Food was left to cool until hand-hot, and Erioglaucine Disodium salt (Sigma) was added at a concentration of 0.01g/ml. Larvae were collected and washed with distilled water in a nine-well glass dissection plate, then added to the coloured food for 30 minutes. Larvae were removed and washed to remove traces of coloured food. Single larvae were then placed in 1.5ml Eppendorf tubes and snap frozen on dry ice, ready for quantification. Frozen samples were lysed in 100µl of distilled water using a pestle, and spun at 4°C at 10,000rpm for seven minutes to remove tissue fragments. The

supernatant was then collected and 50µl was added to a 96-well tissue culture plate (Falcon). Dye standards at 0.000, 0.003, 0.006, 0.012, 0.025 and 0.050µg/µl were also added to generate a standard curve for dye concentration. The intensity of the dye was analysed using a Tecan Sunrise plate-reader, with OD absorption set at 630nm. The OD value of blank wells from the standard was subtracted from all standards, and these normalised values were used to generate a standard curve. OD values for samples were similarly normalised, and the standard curve was then used to calculate the concentration of the dye in each well. This dye concentration was then multiplied by the volume of the buffer the larva was lysed in (100µl) to provide an absolute value for the mass of the dye ingested by each individual larva.

RNA sequencing

Individual samples were dissected as previously described, including the removal of the anterior of the animal with microscissors to exclude the mouthparts and spiracles. As soon as viscera were removed cuticles were frozen in a collection Eppendorf placed on dry ice.

RNA from 30 cuticles per sample was extracted using QIAGEN RNA extraction kits with DNAse treatment, with tissue dissociated using a pestle and mortar and then by QIAshredder column (QIAGEN). RNA quality was checked on a Bioanalyzer, and quantity was checked using a NanoDrop spectrophotometer.

Suitable RNA samples were passed to the Beatson Molecular Technology Service, who performed cDNA library preparation and ran the RNAseq on the Illumina GAIIx sequencer. Raw data was processed by the Beatson Institute Computational Biology group, who analysed the data to generate tables of all genes detected in the RNAseq, and the Log2 fold change of gene expression in the cuticles of Ras^{V12}, $scrib^{1}$ tumour-bearing larvae as opposed to the cuticles from the w^{1118} control. Heatmaps were generated using the MeV software. The read counts of genes of interest were mean-centred to provide a comparable measure of up- or downregulation of gene expression in the cuticles of Ras^{V12}, $scrib^{1}$ tumour-bearing, or w^{1118} control larvae. The table containing full RNAseq data can be found in Table S1.

Statistics and reproducibility

Graphs were generated using GraphPad Prism 6. t test was for two-group comparisons and one-way ANOVA with Tukey or Dunnett post-hoc corrections was used for comparison of multiple samples. Relevant p-values are included in figure legends. With the exception of the data in Figure 6K and Figure S4B all experiments were repeated 2 or 3 times and contain tissue samples from at least 10 animals (n) per repeat. Data in Figure 6K and S4B corresponds to biological duplicated with a total of 8-13 animals. Each dot in dot plot graphs correspond to an individual sample (n).

Acknowledgements

We would like to thank, Bloomington, VDRC and DSHB for lines and reagents. We are thankful to Core Services and Advanced Technologies at the Cancer Research UK Beatson Institute (C596/A17196), with particular thanks to Beatson Advanced Imaging Resource. We are grateful to Federica Parisi, Ross Cagan, Susumu Hirabayashi, and Owen Sansom for discussions and advice throughout the development of this project. We thank William Clark, Gabriela Kalna and Ann Hedley for the production and analysis of the RNAseq data.

In loving memory of Marcos Vidal (1974-2016).

Funding information

J.A.H, J.P.P and Y.Y were supported by Cancer Research UK core funding through the CRUK Beatson Institute (A17196). J.B.C is a Sir Henry Dale Fellow jointly funded by the Wellcome Trust and the Royal Society (Grant Number 104103/Z/14/Z).

The Funders had no involvement in the design or development of this work.

Author Contribution

J.A.H. and J.P.P. designed and performed experiments and analysed the data. Y.Y. provided overall technical assistance and performed RT-qPCRs. M.V. and J.B.C. conceptualised the study, designed experiments, analysed the data and supervised the project. J.A.H., J.P.P. and J.B.C. wrote the manuscript.

Conflict of interest

The authors declare no conflict of interests.

Data and material availability

All data supporting the findings of this study will be available from public repositories (DOI to be provided at the time of publication). RNA sequencing data including all raw sequence files and processed files have been deposited in the Gene Expression Omnibus under accession number GSE178332 and can be accessed through the following link:

https://www.ncbi.nlm.nih.gov/geo/query/acc.cgi?acc=GSE178332.

References

1. Fearon, K., et al., *Definition and classification of cancer cachexia: an international consensus.* Lancet Oncol, 2011. **12**(5): p. 489-95.
2. Couch, M., et al., *Cancer cachexia syndrome in head and neck cancer patients: part I. Diagnosis, impact on quality of life and survival, and treatment.* Head Neck, 2007. **29**(4): p. 401-11.
3. von Haehling, S. and S.D. Anker, *Cachexia as major underestimated unmet medical need: Facts and numbers.* International Journal of Cardiology, 2012. **161**(3): p. 121-123.
4. Donald W Kufe, R.E.P., Ralph R Weichselbaum, Robert C Bast, Jr, Ted S Gansler, James F Holland, and Emil Frei, III, ed. *Holland-Frei Cancer Medicine, 6th edition*. 2003, BC Decker.
5. de Matos-Neto, E.M., et al., *Systemic Inflammation in Cachexia – Is Tumor Cytokine Expression Profile the Culprit?* Frontiers in Immunology, 2015. **6**: p. 629.
6. Wallengren, O., K. Lundholm, and I. Bosaeus, *Diagnostic criteria of cancer cachexia: relation to quality of life, exercise capacity and survival in unselected palliative care patients.* Support Care Cancer, 2013. **21**(6): p. 1569-77.
7. Andreyev, H.J., et al., *Why do patients with weight loss have a worse outcome when undergoing chemotherapy for gastrointestinal malignancies?* Eur J Cancer, 1998. **34**(4): p. 503-9.
8. O'Gorman, P., D.C. McMillan, and C.S. McArdle, *Impact of weight loss, appetite, and the inflammatory response on quality of life in gastrointestinal cancer patients.* Nutr Cancer, 1998. **32**(2): p. 76-80.
9. Lok, C., *Cachexia: The last illness.* Nature, 2015. **528**(7581): p. 182-3.
10. Fearon, K.C.H. and A.G.W. Moses, *Cancer cachexia.* International Journal of Cardiology, 2002. **85**(1): p. 73-81.
11. Dewys, W.D., et al., *Prognostic effect of weight loss prior to chemotherapy in cancer patients. Eastern Cooperative Oncology Group.* Am J Med, 1980. **69**(4): p. 491-7.

12. Bachmann, J., et al., *Pancreatic cancerrelated cachexia: influence on metabolism and correlation to weight loss and pulmonary function.* BMC Cancer, 2009. **9**: p. 255-255.
13. Del Ferraro, C., et al., *Management of Anorexia-Cachexia in Late Stage Lung Cancer Patients.* Journal of hospice and palliative nursing : JHPN : the official journal of the Hospice and Palliative Nurses Association, 2012. **14**(6): p. 10.1097/NJH.0b013e31825f3470.
14. Monitto, C.L., et al., *Differential gene expression in a murine model of cancer cachexia.* Am J Physiol Endocrinol Metab, 2001. **281**(2): p. E289-97.
15. Bennani-Baiti, N. and D. Walsh, *Animal models of the cancer anorexia–cachexia syndrome.* Supportive Care in Cancer, 2011. **19**(9): p. 1451-1463.
16. Bilder, D., M. Li, and N. Perrimon, *Cooperative Regulation of Cell Polarity and Growth by Drosophila Tumor Suppressors.* Science, 2000. **289**(5476): p. 113-116.
17. Wu, M., J.C. Pastor-Pareja, and T. Xu, *Interaction between Ras(V12) and scribble clones induces tumour growth and invasion.* Nature, 2010. **463**(7280): p. 545-548.
18. Pagliarini, R.A. and T. Xu, *A genetic screen in Drosophila for metastatic behavior.* Science, 2003. **302**(5648): p. 1227-31.
19. Parisi, F., et al., *Transformed Epithelia Trigger Non-Tissue-Autonomous Tumor Suppressor Response by Adipocytes via Activation of Toll and Eiger/TNF Signaling.* Cell Reports, 2014. **6**(5): p. 855-867.
20. Pastor-Pareja, J.C., M. Wu, and T. Xu, *An innate immune response of blood cells to tumors and tissue damage in Drosophila.* Disease Models & Mechanisms, 2008. **1**(2-3): p. 144-154.
21. Cordero, J.B., et al., *Oncogenic Ras Diverts a Host TNF Tumor Suppressor Activity into Tumor Promoter.* Developmental cell, 2010. **18**(6): p. 999-1011.
22. Katheder, N.S., et al., *Microenvironmental autophagy promotes tumour growth.* Nature, 2017. **541**(7637): p. 417-420.
23. Kwon, Y., et al., *Systemic Organ Wasting Induced by Localized Expression of the Secreted Insulin/IGF Antagonist ImpL2.* Developmental Cell, 2015. **33**(1): p. 36-46.
24. Figueroa-Clarevega, A. and D. Bilder, *Malignant Drosophila tumors interrupt insulin signaling to induce cachexia-like wasting.* Developmental cell, 2015. **33**(1): p. 47-55.
25. Lee, J., et al., *Tumors overcome the action of the wasting factor ImpL2 by locally elevating Wnt/Wingless.* Proc Natl Acad Sci U S A, 2021. **118**(23).
26. Yeom, E., et al., *Tumour-derived Dilp8/INSL3 induces cancer anorexia by regulating feeding neuropeptides via Lgr3/8 in the brain.* Nat Cell Biol, 2021. **23**(2): p. 172-183.
27. Newton, H., et al., *Systemic muscle wasting and coordinated tumour response drive tumourigenesis.* Nat Commun, 2020. **11**(1): p. 4653.
28. Humbert, P.O., et al., *Control of tumourigenesis by the Scribble/Dlg/Lgl polarity module.* Oncogene, 2008. **27**(55): p. 6888-907.
29. Bilder, D. and N. Perrimon, *Localization of apical epithelial determinants by the basolateral PDZ protein Scribble.* Nature, 2000. **403**(6770): p. 676-80.

30. Brumby, A.M. and H.E. Richardson, *scribble mutants cooperate with oncogenic Ras or Notch to cause neoplastic overgrowth in Drosophila.* The EMBO Journal, 2003. **22**(21): p. 5769-5779.
31. Oh, H. and K.D. Irvine, *In vivo analysis of Yorkie phosphorylation sites.* Oncogene, 2009. **28**(17): p. 1916-1927.
32. Stephens, N.A., et al., *Intramyocellular lipid droplets increase with progression of cachexia in cancer patients.* Journal of Cachexia, Sarcopenia and Muscle, 2011. **2**(2): p. 111-117.
33. Garelli, A., et al., *Imaginal Discs Secrete Insulin-Like Peptide 8 to Mediate Plasticity of Growth and Maturation.* Science, 2012. **336**(6081): p. 579-582.
34. Douglas, R.G. and J.H. Shaw, *Metabolic effects of cancer.* Br J Surg, 1990. **77**(3): p. 246-54.
35. Morrison, S.D., *Control of food intake in cancer cachexia: A challenge and a tool.* Physiology & Behavior, 1976. **17**(4): p. 705-714.
36. Tisdale, M.J., *Cancer cachexia: Metabolic alterations and clinical manifestations.* Nutrition, 1997. **13**(1): p. 1-7.
37. Gullett, N.P., et al., *Nutritional Interventions for Cancer-induced Cachexia.* Current problems in cancer, 2011. **35**(2): p. 58-90.
38. Szuperák, M., et al., *Feedback regulation of Drosophila BMP signaling by the novel extracellular protein Larval Translucida.* Development, 2011. **138**(4): p. 715-724.
39. Baracos, V.E., et al., *Activation of the ATP-ubiquitin-proteasome pathway in skeletal muscle of cachectic rats bearing a hepatoma.* Am J Physiol, 1995. **268**(5 Pt 1): p. E996-1006.
40. Cruz, B., A. Oliveira, and M.C.C. Gomes-Marcondes, *L-leucine dietary supplementation modulates muscle protein degradation and increases pro-inflammatory cytokines in tumour-bearing rats.* Cytokine, 2017. **96**: p. 253-260.
41. Fujita, J., et al., *Anti-interleukin-6 receptor antibody prevents muscle atrophy in colon-26 adenocarcinoma-bearing mice with modulation of lysosomal and ATP-ubiquitin-dependent proteolytic pathways.* Int J Cancer, 1996. **68**(5): p. 637-43.
42. Smith, K.L. and M.J. Tisdale, *Mechanism of muscle protein degradation in cancer cachexia.* Br J Cancer, 1993. **68**(2): p. 314-8.
43. VanderVeen, B.N., D.K. Fix, and J.A. Carson, *Disrupted Skeletal Muscle Mitochondrial Dynamics, Mitophagy, and Biogenesis during Cancer Cachexia: A Role for Inflammation.* Oxid Med Cell Longev, 2017. **2017**: p. 3292087.
44. Yuan, L., et al., *Muscle-specific E3 ubiquitin ligases are involved in muscle atrophy of cancer cachexia: An in vitro and in vivo study.* Oncol Rep, 2015. **33**(5): p. 2261-2268.
45. Bonetto, A., et al., *JAK/STAT3 pathway inhibition blocks skeletal muscle wasting downstream of IL-6 and in experimental cancer cachexia.* American Journal of Physiology - Endocrinology And Metabolism, 2012. **303**(3): p. E410-E421.
46. Baltgalvis, K.A., et al., *Muscle Wasting and Interleukin-6-Induced Atrogin-I Expression in the Cachectic Apc(Min/+) Mouse.* Pflugers Archiv : European journal of physiology, 2009. **457**(5): p. 989-1001.
47. Miller, A., et al., *Blockade of the IL-6 trans-signalling/STAT3 axis suppresses cachexia in Kras-induced lung adenocarcinoma.* Oncogene, 2017. **36**(21): p. 3059-3066.

48. Pettersen, K., et al., *Cancer cachexia associates with a systemic autophagy-inducing activity mimicked by cancer cell-derived IL-6 trans-signaling.* Scientific Reports, 2017. **7**: p. 2046.
49. Martignoni, M.E., et al., *Role of mononuclear cells and inflammatory cytokines in pancreatic cancer-related cachexia.* Clin Cancer Res, 2005. **11**(16): p. 5802-8.
50. Moses, A.G., et al., *Pro-inflammatory cytokine release by peripheral blood mononuclear cells from patients with advanced pancreatic cancer: relationship to acute phase response and survival.* Oncol Rep, 2009. **21**(4): p. 1091-5.
51. Narsale, A.A. and J.A. Carson, *Role of IL-6 In Cachexia – Therapeutic Implications.* Current opinion in supportive and palliative care, 2014. **8**(4): p. 321-327.
52. Pop, V.V., et al., *IL-6 roles - Molecular pathway and clinical implication in pancreatic cancer - A systemic review.* Immunol Lett, 2017. **181**: p. 45-50.
53. Goldberg, R.M., et al., *Pentoxifylline for treatment of cancer anorexia and cachexia? A randomized, double-blind, placebo-controlled trial.* J Clin Oncol, 1995. **13**(11): p. 2856-9.
54. Yakovenko, A., M. Cameron, and J.G. Trevino, *Molecular therapeutic strategies targeting pancreatic cancer induced cachexia.* World J Gastrointest Surg, 2018. **10**(9): p. 95-106.
55. Kanda, H., et al., *Wengen, a member of the Drosophila tumor necrosis factor receptor superfamily, is required for Eiger signaling.* J Biol Chem, 2002. **277**(32): p. 28372-5.
56. Kauppila, S., et al., *Eiger and its receptor, Wengen, comprise a TNF-like system in Drosophila.* Oncogene, 2003. **22**(31): p. 4860-7.
57. Belizario, J.E., et al., *Skeletal muscle wasting and renewal: a pivotal role of myokine IL-6.* Springerplus, 2016. **5**: p. 619.
58. Onesti, J.K. and D.C. Guttridge, *Inflammation based regulation of cancer cachexia.* Biomed Res Int, 2014. **2014**: p. 168407.
59. Potter, C.J., et al., *The Q system: a repressible binary system for transgene expression, lineage tracing, and mosaic analysis.* Cell, 2010. **141**(3): p. 536-48.
60. Brand, A.H. and N. Perrimon, *Targeted gene expression as a means of altering cell fates and generating dominant phenotypes.* Development, 1993. **118**(2): p. 401-15.

Figure legends

Figure 1. Cachectic wasting is dependent on tumour genotype. (A) Schematic of experimental approach used to assess tumour volume, muscle wasting and IMLDs. (**B-E**) Imaginal tissues stained with DAPI. Normal wing disc at 6 days AED (w^{1118}) (**B**). Hyperplastic tumour at 6 days AED (*rotund>Yki*^{S168A}) **(C),** non-invasive neoplastic tumour at 12 days AED ($dlg^{40.2}$) (**D**) and MARCM-generated eye invasive neoplastic tumour at 12 days AED (Ras^{V12}, $scrib^{1}$) (**E**). (**F**) Tissue volume quantification. **(G-J**) Cuticles with muscle actin stained with Phalloidin (green) from animals of genotypes and ages as in B-E. **(K**) Quantification of the percentage of cuticle covered by muscle**. (L-O")** 5th segment of the 7th ventral muscle, stained with DAPI (blue), Phalloidin (green), and LipidTOX to visualize lipids (red and grey) in body wall muscles from animals of genotypes and ages as in B-E. All panels denoted (') show lipid staining only. All panels denoted (") show a transversal orthographic view of muscle with a 2X zoom, stained with Phalloidin and LipidTOX. **(P**) Quantification of the frequency of IMLDs in the 5th segment of the 7th ventral muscle, expressed as a ratio over the area of that muscle. All graphs show one-way ANOVA with Tukey post-hoc correction. ns: non-significant, $p \geq 0.05$; *$p \leq 0.05$; **$p \leq 0.01$; ****$p \leq 0.0001$.

Figure 2. Tumour size is not sufficient to drive cachexia. (A,B) Tumours stained with DAPI. *rotund>Yki*^{S168A} tumours induced in an ecd^{1} mutant background **(A)**, and MARCM eye Ras^{V12}, $scrib^{1}$ tumours (**B**), both at 11 days AED. **(C,D)** Cuticles from animals as in A and B, with muscle actin stained with Phalloidin (green). **(E-F")** 5th segment of the 7th ventral muscle, stained with DAPI (blue), Phalloidin (green), and LipidTOX (red or grey). Animal ages and genotypes as in A and B. Panels denoted (') show lipid staining only. Panels denoted (") show a transversal orthographic view of muscle with a 2X zoom. **(G)** Tissue volume quantification. **(H**) Quantification of the percentage of the cuticle covered by muscle. **I**, Quantification of the frequency of IMLDs in the 5th segment of the 7th ventral muscle, expressed as a ratio over the area of that muscle. All graphs show t test. ns: non-significant, $p \geq 0.05$; ****$p \leq 0.0001$.

Figure 3. Starvation or bloating are not sufficient to drive cachexia. (A) Schematic of the approach for assessment of larval feeding. **(B, C**) Quantification of dye levels consumed by larvae of the indicated genotypes. **(D-I**) Images of whole larvae. Normal (w^{1118}) larvae at 3 (**D**) and 6 (**E**) days AED. Tumour-free bloated larvae with ubiquitous *tubulin>Gal4*-driven expression of Itl^{IR} at 3 (**F**) and 7 (**G**) days AED.

Ras^{V12}, *scrib*^{1} tumour-bearing larvae at 8 (**H**) and 12 (**I**) days AED. **(J-L**) Imaginal tissues stained with DAPI. Normal eye-antennal disc at 6 days AED (*w*^{1118}) (**J**), eye-antennal disc at 7 days AED (*tub>Itl*^{IR}) (**K**), and invasive neoplastic eye tumours at 12 days AED (*Ras*^{V12}, *scrib*^{1}) (**L**). **(M-O**) Cuticles with muscle actin stained with Phalloidin, animals of ages and genotypes as described for J-L. **(P-R"**) 5th segment of the 7th ventral muscle, stained with DAPI, Phalloidin, and LipidTOX. Animal ages and genotypes as described for J-L. All panels denoted (') show lipid staining only. All panels denoted (") show a transversal orthographic view of muscle with a 2X zoom. **(S**) Quantification of bloating expressed as mean mass of haemolymph extracted per larvae. **(T**) Quantification of the percentage of the cuticle covered by muscle. All graphs show one-way ANOVA with Tukey post-hoc correction. ns: non-significant, $p \geq 0.05$; *$p \leq 0.05$; ***$p \leq 0.001$; ****$p \leq 0.0001$.

Figure 4. Molecular characterization of cachectic muscles from tumour bearing larvae. (A) Frequency of up- and downregulated expression of genes identified in an RNAseq from cuticles of normal (*w*^{1118}) and MARCM *Ras*^{V12}, *scrib*^{1} tumour-bearing animals. **(B**) List of GO terms enriched in up- and downregulated gene sets from RNAseq**. (C)** List of pathway terms enriched in up- and downregulated gene sets from RNAseq**. (D)** Heatmap of relative expression levels of JAK/STAT pathway genes from RNAseq. Heatmap colour intensity displays $\log_2$-fold change values relative to the mean gene expression level across both genotypes.

Figure 5. Generation of a dual driver system for independent genetic manipulation of skeletal muscle and larval imaginal discs. (A) Schematic of the genetic components of a dual driver system used for genetic manipulation of muscle skeletal muscle in larvae bearing eye/antennal disc control or *Ras*^{V12}, *scrib*^{1} clones. **(B)** 10-day-old larvae with dual driver system generated *scrib*^{1}; *Ras*^{V12} clones (red) and muscle specific concomitant overexpression of a *UAS-gfp* transgene (*green*). Boxed area delineates magnified view (bottom panel) of muscle with regions showing signs of muscle fibre loss. **(C, D)** Whole animal view (left panels) and eye/antennal imaginal discs (right panels) from larvae with dual driver system generated imaginal disc control (7-day-old C) or *scrib*^{1}; *Ras*^{V12} clones (10-day-old D) (red) and muscle specific concomitant overexpression of a *UAS-gfp* transgene (*green*).

Figure 6. Muscle JAK/STAT and TNF-α signalling drives tissue wasting. (A-C) mRNA expression levels of the JAK/STAT pathway target *Socs36E* (A), the TNF-

α/Egr receptor *wgn* (B) and the *Atrogin 1* homologue *CG116758* (C) in skeletal muscle from 7-day-old wild type larvae (w^{1118}) or larvae with dual driver system (DDS) generated control (Tumour free) or $scrib^{1}$; Ras^{V12} clones (Tumour bearing). **(D-J**) Cuticles from larvae with DDS generated control clones (Tumour free; 6 day-old) (D) or $scrib^{1}$; Ras^{V12} clones (Tumour bearing) with muscle specific concomitant overexpression of a control transgene (*gfp*), *stat RNAi* (*stat-IR*) or *wgn RNAi* (*wgn-IR*) (E-J). Cuticles of tumour bearing animals were assessed at 10 days (E-G) and 12 days (H-J) of larval age. Muscle actin was stained Phalloidin (green). **(K)** Quantification of the percentage of cuticle covered by muscle in larvae of genotypes and ages as in D-J**.** All graphs show one-way ANOVA with Tukey post-hoc correction. *$p \leq 0.05$; ***$p \leq 0.001$; ****$p \leq 0.0001$.

Figure 1

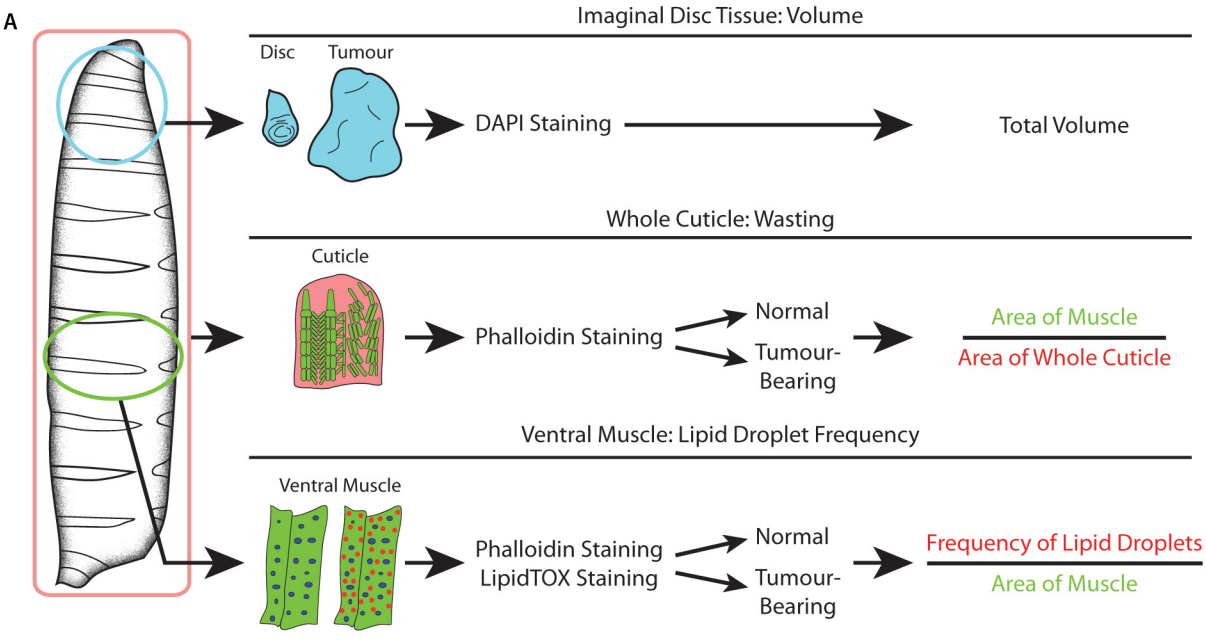
A
Imaginal Disc Tissue: Volume
Disc
Tumour
DAPI Staining
Total Volume
Whole Cuticle: Wasting
Cuticle
Phalloidin Staining
Normal
Tumour-Bearing
Area of Muscle
Area of Whole Cuticle
Ventral Muscle: Lipid Droplet Frequency
Ventral Muscle
Phalloidin Staining
LipidTOX Staining
Normal
Tumour-Bearing
Frequency of Lipid Droplets
Area of Muscle

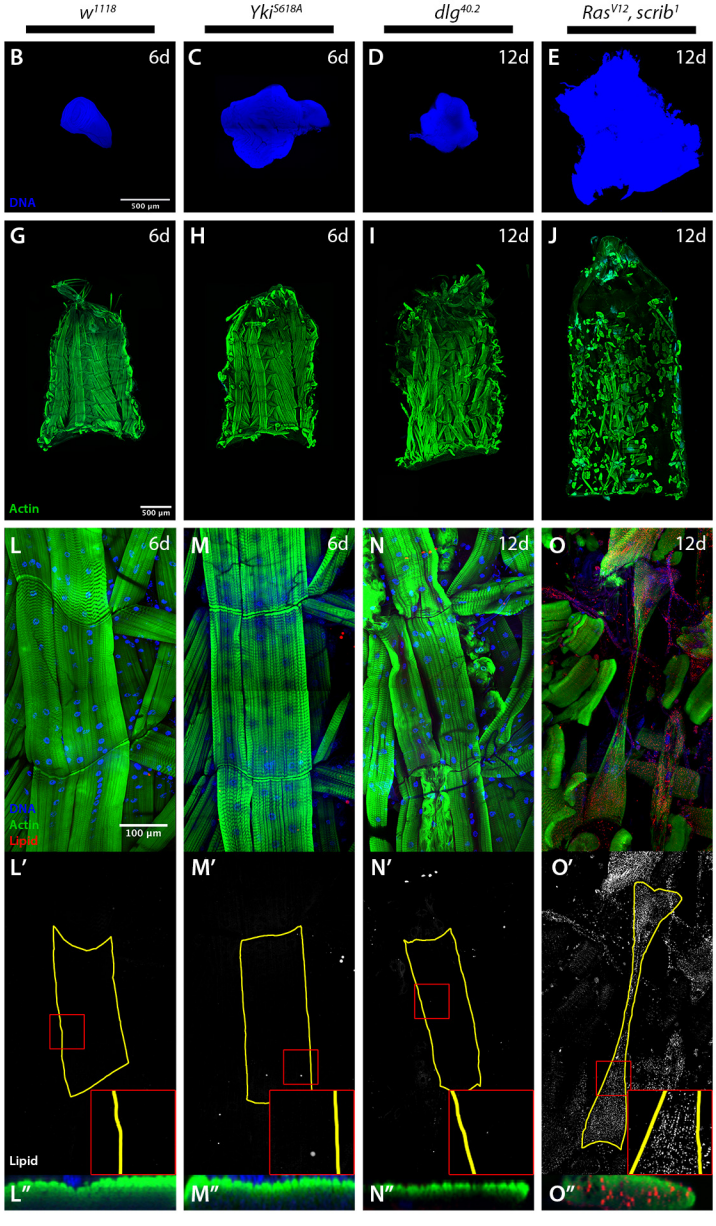
w1118
YkiS618A
dlg40.2
RasV12, scrib1
B 6d
C 6d
D 12d
E 12d
DNA
500 µm
G 6d
H 6d
I 12d
J 12d
Actin
500 µm
L 6d
M 6d
N 12d
O 12d
DNA
Actin
Lipid
100 µm
L′
M′
N′
O′
Lipid
L″
M″
N″
O″

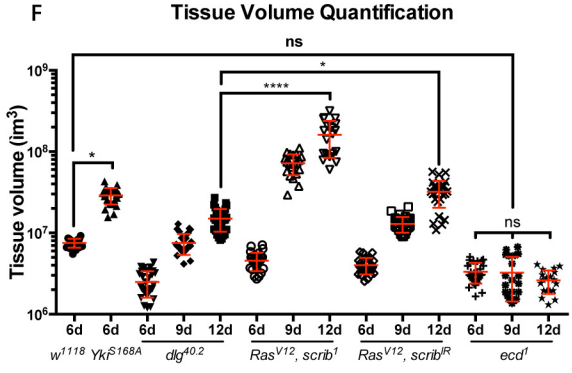
F
Tissue Volume Quantification
Tissue volume (im3)
ns
*
****
*
ns
6d 6d 6d 9d 12d 6d 9d 12d 6d 9d 12d 6d 9d 12d
w1118 YkiS168A dlg40.2 RasV12, scrib1 RasV12, scribIR ecd1

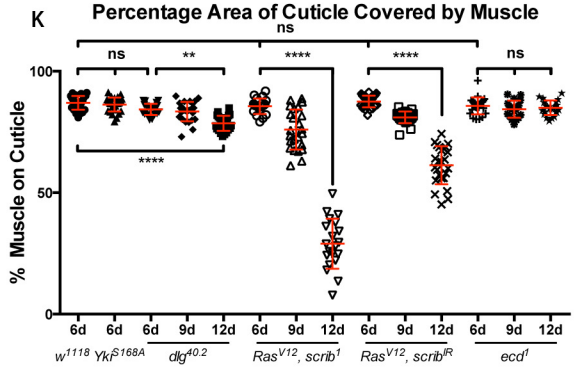
K
Percentage Area of Cuticle Covered by Muscle
% Muscle on Cuticle
ns
ns
**
****
****
****
ns
6d 6d 6d 9d 12d 6d 9d 12d 6d 9d 12d 6d 9d 12d
w1118 YkiS168A dlg40.2 RasV12, scrib1 RasV12, scribIR ecd1

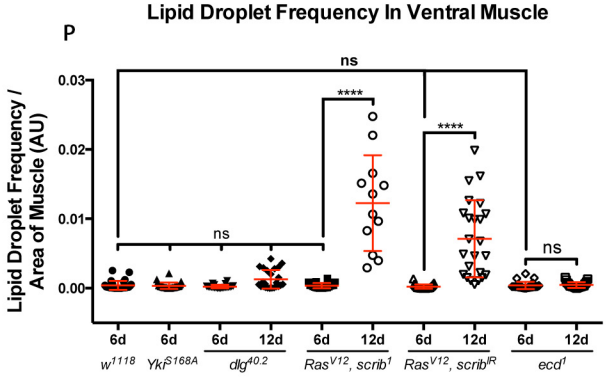
P
Lipid Droplet Frequency In Ventral Muscle
Lipid Droplet Frequency / Area of Muscle (AU)
ns
****
****
ns
ns
6d 6d 6d 12d 6d 12d 6d 12d 6d 12d
w1118 YkiS168A dlg40.2 RasV12, scrib1 RasV12, scribIR ecd1

Figure 2

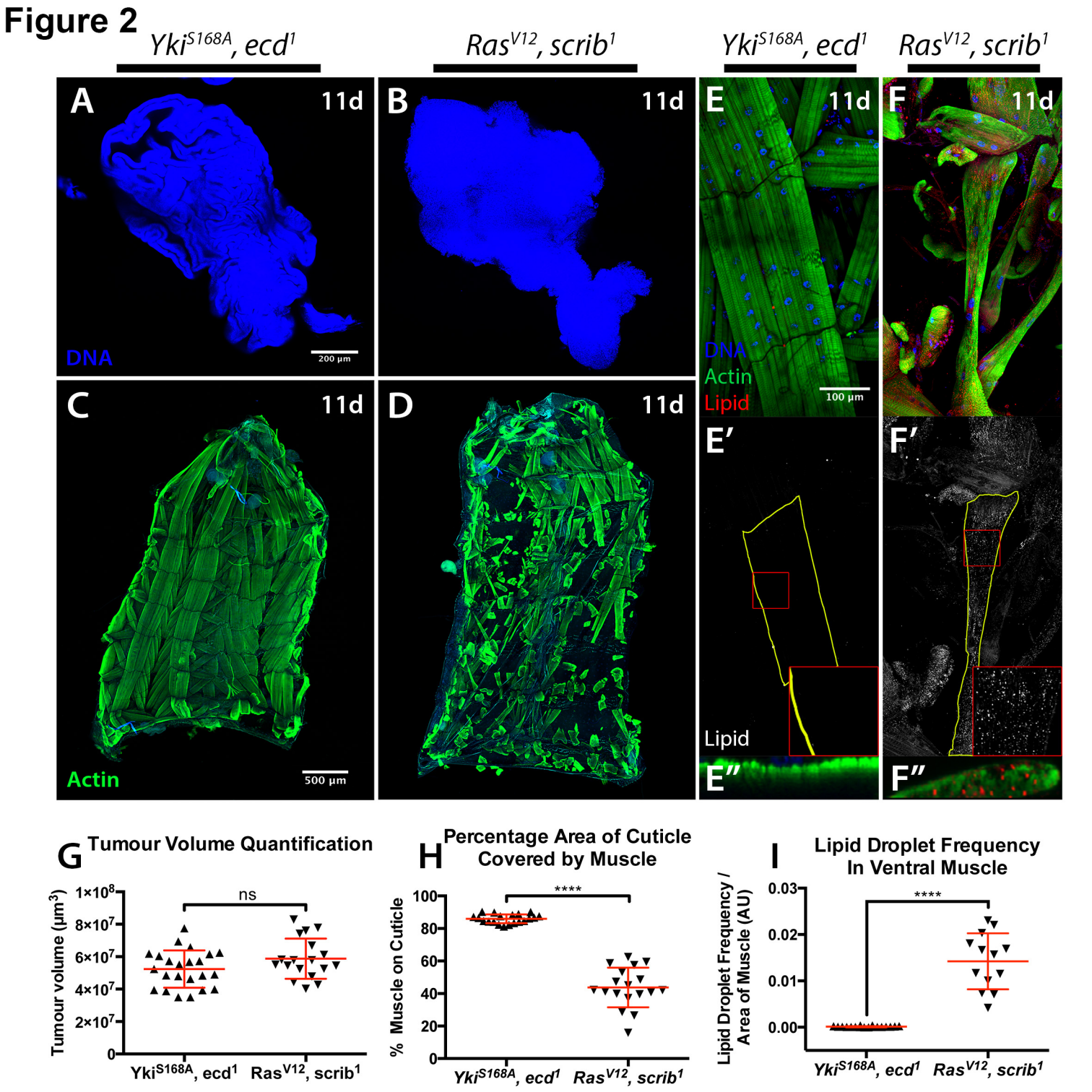
Yki^{S168A}, ecd^{1}
Ras^{V12}, scrib^{1}
Yki^{S168A}, ecd^{1}
Ras^{V12}, scrib^{1}
A
11d
DNA
200 µm
B
11d
C
11d
Actin
500 µm
D
11d
E
11d
DNA
Actin
Lipid
100 µm
F
11d
E′
Lipid
F′
E″
F″
G
Tumour Volume Quantification
Tumour volume (µm^3)
1×10^8
8×10^7
6×10^7
4×10^7
2×10^7
0
ns
Yki^{S168A}, ecd^{1}
Ras^{V12}, scrib^{1}
H
Percentage Area of Cuticle Covered by Muscle
% Muscle on Cuticle
100
80
60
40
20
0
****
Yki^{S168A}, ecd^{1}
Ras^{V12}, scrib^{1}
I
Lipid Droplet Frequency In Ventral Muscle
Lipid Droplet Frequency / Area of Muscle (AU)
0.03
0.02
0.01
0.00
****
Yki^{S168A}, ecd^{1}
Ras^{V12}, scrib^{1}

Figure 3

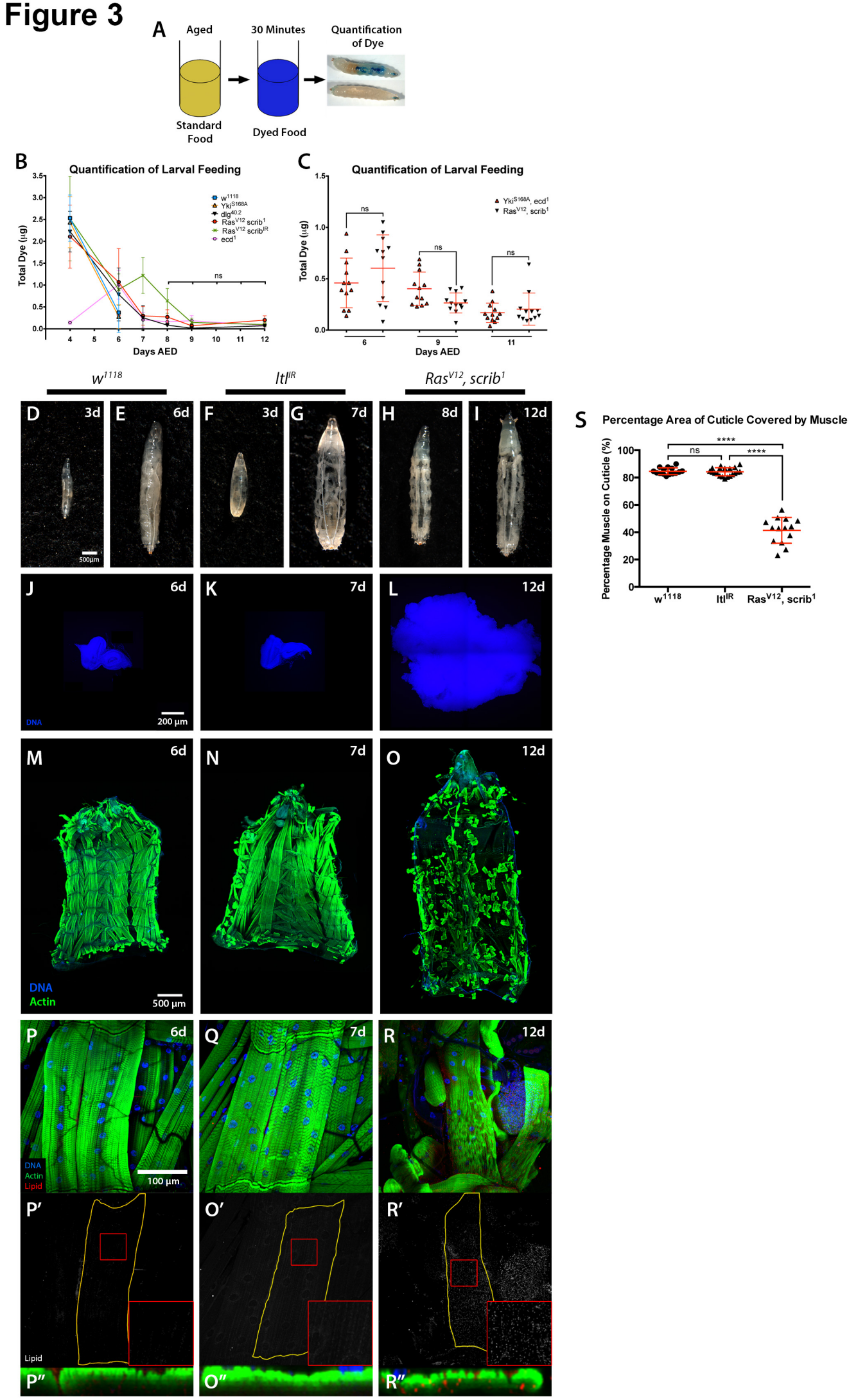
A
Aged
30 Minutes
Quantification of Dye
Standard Food
Dyed Food
B
Quantification of Larval Feeding
Total Dye (µg)
Days AED
ns
C
Quantification of Larval Feeding
Total Dye (µg)
Days AED
ns
w1118
Ykis168A
dlg40.2
RasV12 scrib1
RasV12 scribIR
ecd1
Ykis168A, ecd1
RasV12, scrib1
w1118
ItlIR
RasV12, scrib1
D 3d
E 6d
F 3d
G 7d
H 8d
I 12d
500µm
J 6d
K 7d
L 12d
DNA
200 µm
M 6d
N 7d
O 12d
DNA
Actin
500 µm
P 6d
Q 7d
R 12d
DNA
Actin
Lipid
100 µm
P′
O′
R′
Lipid
P″
O″
R″
S
Percentage Area of Cuticle Covered by Muscle
Percentage Muscle on Cuticle (%)
ns
****
****
w1118
ItlIR
RasV12, scrib1

Figure 4

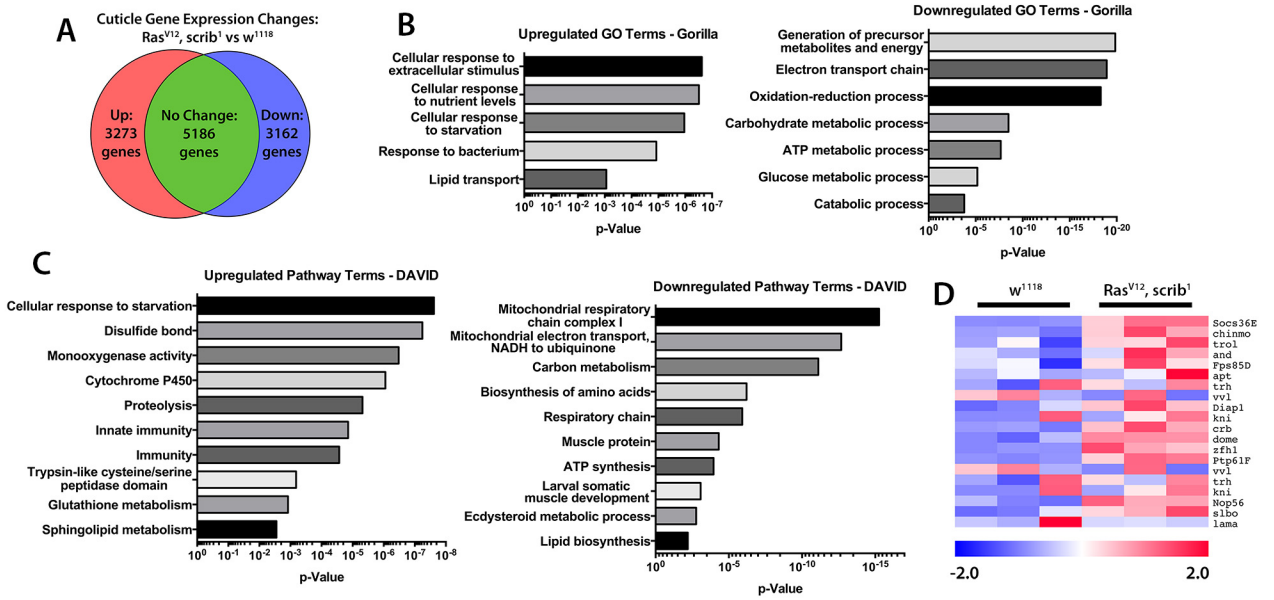
A
Cuticle Gene Expression Changes:
Ras^{V12}, scrib^{1} vs w^{1118}
Up: 3273 genes
No Change: 5186 genes
Down: 3162 genes
B
Upregulated GO Terms - Gorilla
Cellular response to extracellular stimulus
Cellular response to nutrient levels
Cellular response to starvation
Response to bacterium
Lipid transport
10^{0} 10^{-1} 10^{-2} 10^{-3} 10^{-4} 10^{-5} 10^{-6} 10^{-7}
p-Value
Downregulated GO Terms - Gorilla
Generation of precursor metabolites and energy
Electron transport chain
Oxidation-reduction process
Carbohydrate metabolic process
ATP metabolic process
Glucose metabolic process
Catabolic process
10^{0} 10^{-5} 10^{-10} 10^{-15} 10^{-20}
p-Value
C
Upregulated Pathway Terms - DAVID
Cellular response to starvation
Disulfide bond
Monooxygenase activity
Cytochrome P450
Proteolysis
Innate immunity
Immunity
Trypsin-like cysteine/serine peptidase domain
Glutathione metabolism
Sphingolipid metabolism
10^{0} 10^{-1} 10^{-2} 10^{-3} 10^{-4} 10^{-5} 10^{-6} 10^{-7} 10^{-8}
p-Value
Downregulated Pathway Terms - DAVID
Mitochondrial respiratory chain complex I
Mitochondrial electron transport, NADH to ubiquinone
Carbon metabolism
Biosynthesis of amino acids
Respiratory chain
Muscle protein
ATP synthesis
Larval somatic muscle development
Ecdysteroid metabolic process
Lipid biosynthesis
10^{0} 10^{-5} 10^{-10} 10^{-15}
p-Value
D
w^{1118}
Ras^{V12}, scrib^{1}
Socs36E
chinmo
trol
and
Fps85D
apt
trh
vvl
Diap1
kni
crb
dome
zfh1
Ptp61F
vvl
trh
kni
Nop56
slbo
lama
-2.0
2.0

Figure 5

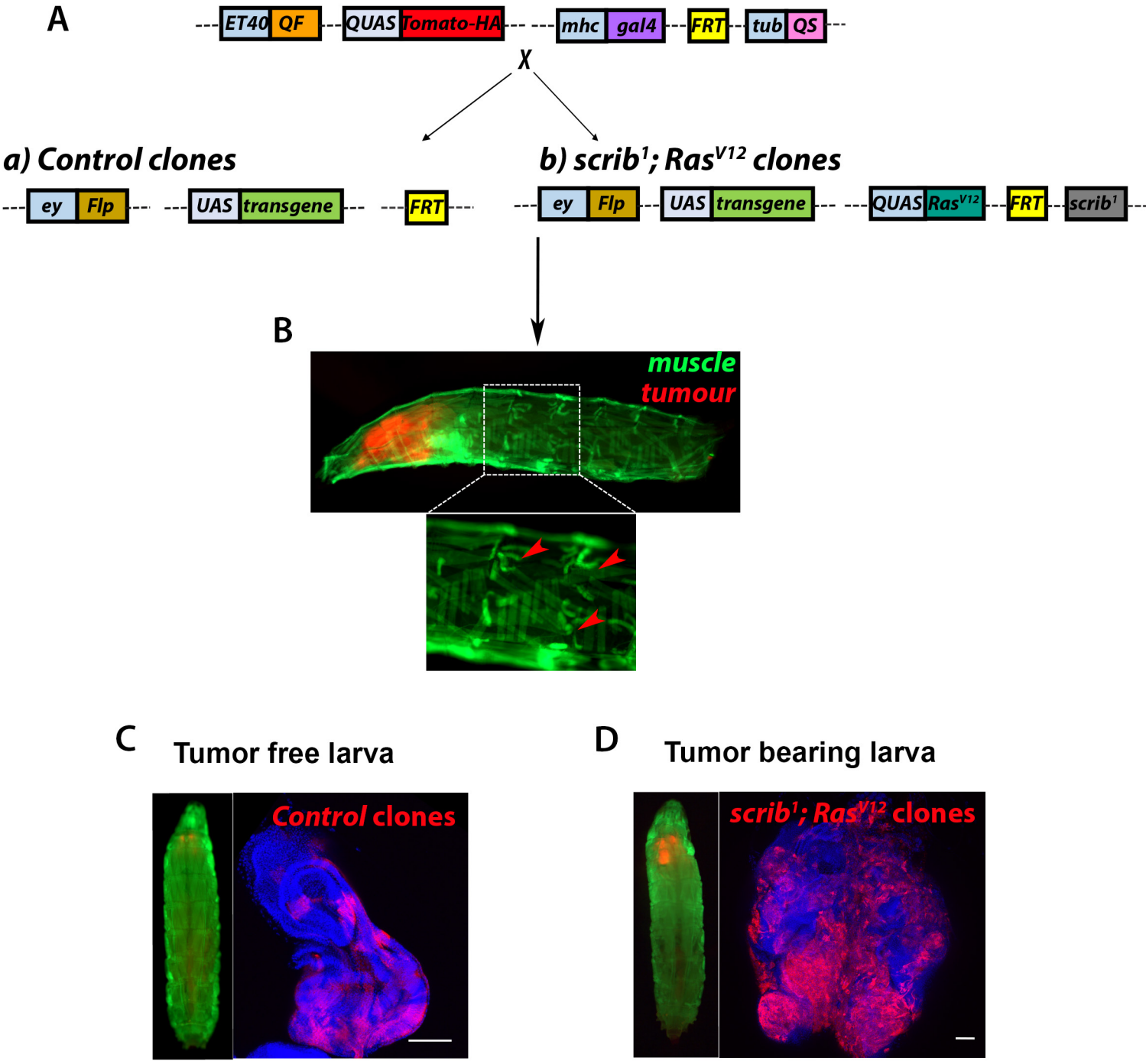
A
ET40
QF
QUAS
Tomato-HA
mhc
gal4
FRT
tub
QS
X
a) Control clones
ey
Flp
UAS
transgene
FRT
b) scrib1; RasV12 clones
ey
Flp
UAS
transgene
QUAS
RasV12
FRT
scrib1
B
muscle
tumour
C
Tumor free larva
Control clones
D
Tumor bearing larva
scrib1; RasV12 clones

Figure 6

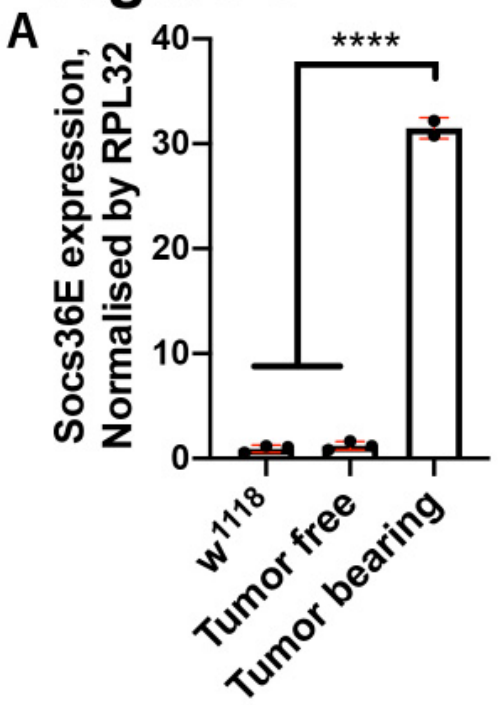
A
Socs36E expression, Normalised by RPL32
****
w1118
Tumor free
Tumor bearing

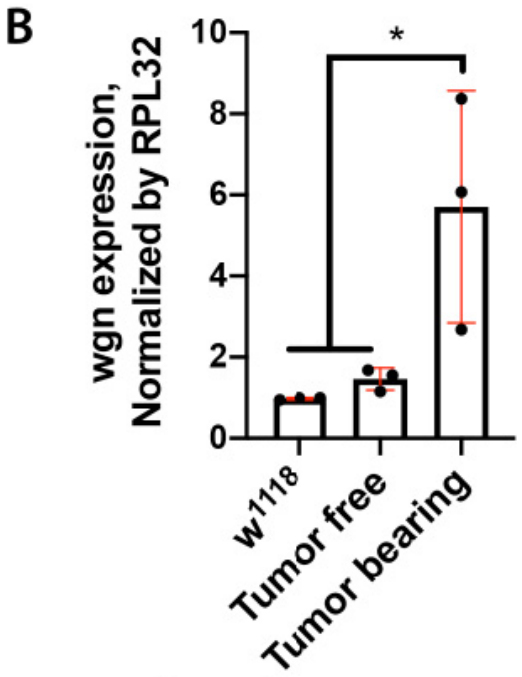
B
wgn expression, Normalized by RPL32
*
w1118
Tumor free
Tumor bearing

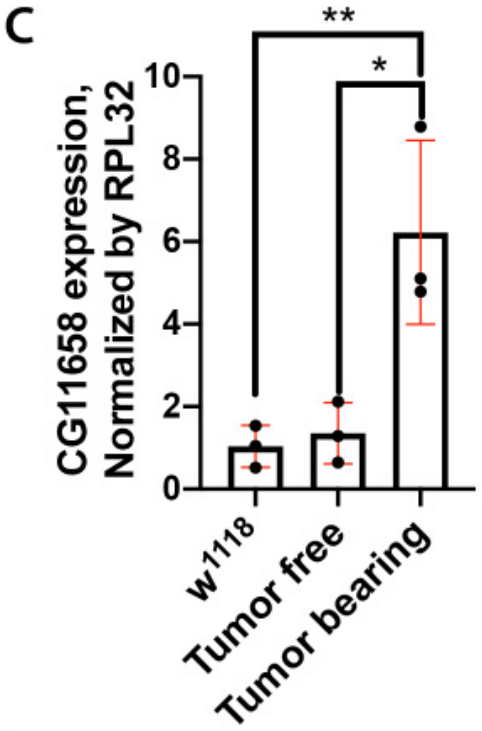
C
CG11658 expression, Normalized by RPL32
**
*
w1118
Tumor free
Tumor bearing

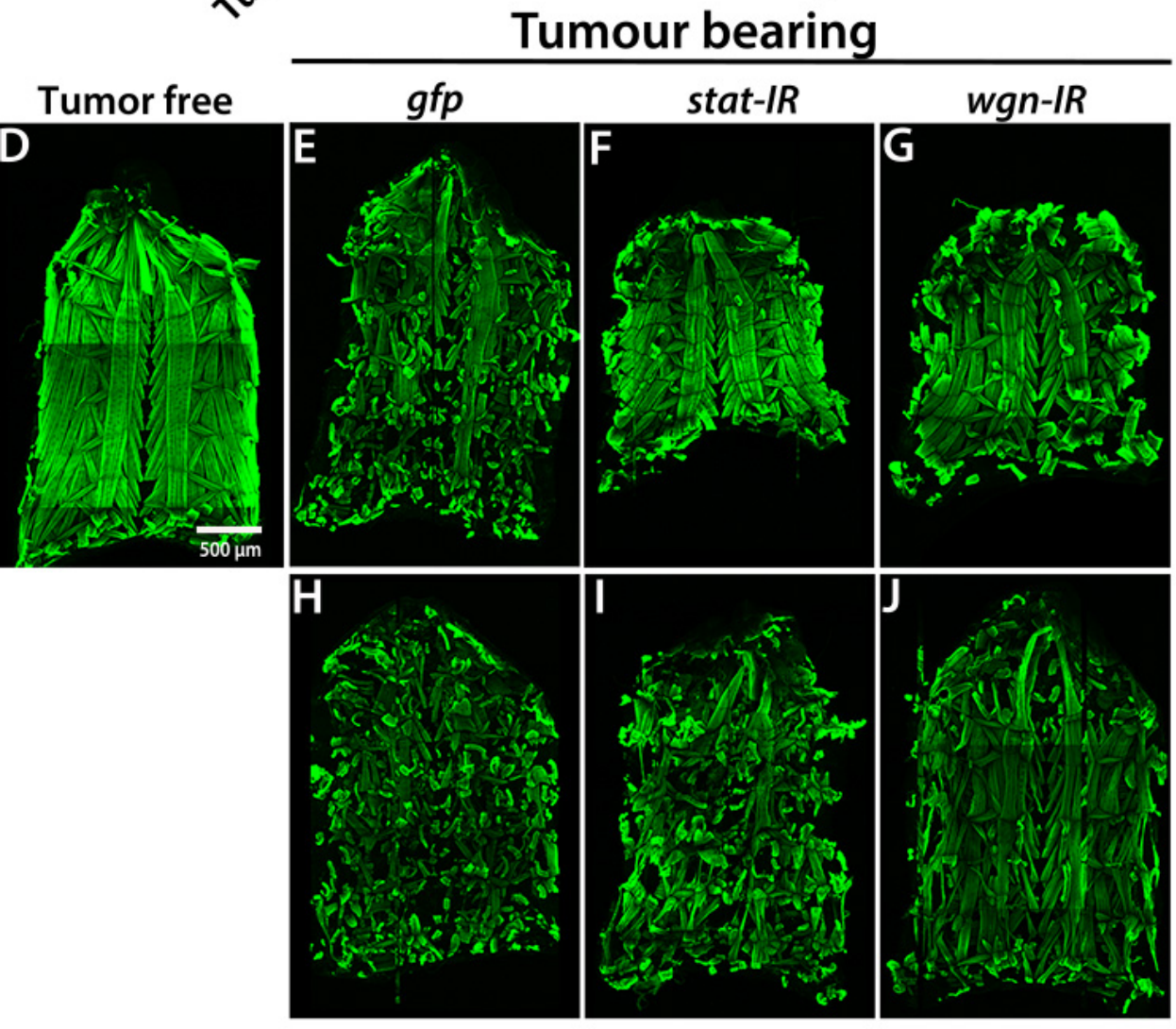
Tumour bearing
Tumor free
gfp
stat-IR
wgn-IR
D
E
F
G
H
I
J
500 µm

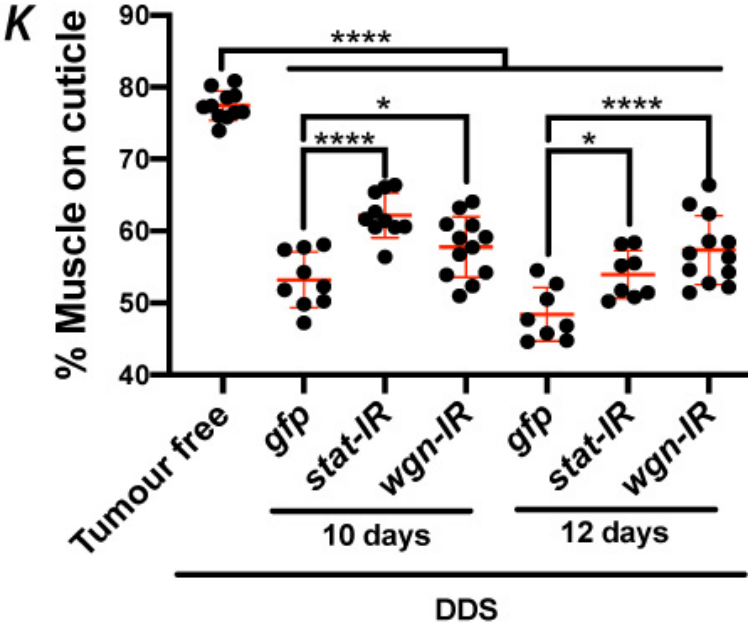
K
% Muscle on cuticle
****
*
****
****
*
Tumour free
gfp
stat-IR
wgn-IR
gfp
stat-IR
wgn-IR
10 days
12 days
DDS